Electronic Supplementary Information

Synergistic Optimization of Electronic and Lattice Structures through Ti-Intercalation and Se-Vacancy Engineering for High-Performance Aluminum Storage

Rongkai Kang,[a] Dongmei Zhang,[a] Han Wang,[a] Boya Zhang,[a] Xingchang Zhang,[a] Guowen Chen,[a] Yiqun Du*[b] and Jianxin Zhang*[a]*

[a] Key Laboratory for Liquid-Solid Structural Evolution and Processing of Materials (Ministry of Education), School of Materials Science and Engineering, Shandong University, Jinan 250061, China.

[b] School of Materials Science and Engineering, University of Jinan, Jinan 250022, China.

* Corresponding authors.

* E-mail: cgw@sdu.edu.cn, mse_duyq@ujn.edu.cn, jianxin@sdu.edu.cn

Experimental

Material synthesis:

Synthesis of $MoSe_2$ and Ti-$MoSe_2$: Sodium molybdate (0.52 g) and sulfuric acid (0.1 M, 3 mL) were added to deionized water (50 mL) during agitation. After that, titanium(IV) sulfate (0.024 g) was added to the solution. Besides, selenium powder (0.4 g) was dissolved in hydrazine hydrate (80%, 10 mL), after which the obtained solution was slowly added to the sodium molybdate solution and continuously agitated for 30 min. The resulting solution was transferred to a Teflon autoclave and held at 200 ℃ for 24 h. After cooling, the sediment was centrifugally washed with deionized water and ethanol, and then dried at 70 ℃ for 12 h in a vacuum oven to obtain the Ti-$MoSe_2$. Similarly, the $MoSe_2$ was prepared in the same method, except for the presence of titanium(IV) sulfate.

Synthesis of $MoSe_{2-x}$ and Ti-$MoSe_{2-x}$: The Ti-$MoSe_2$ powder was transferred into a microwave oven under Ar atmosphere and radiated at 800 W for 15 s to obtain the Ti-$MoSe_{2-x}$. Similarly, $MoSe_{2-x}$ is prepared in the same method, except that the raw material is $MoSe_2$ powder.

Material characterizations:

The X-ray diffraction (XRD, Rigaku Ultima IV) was used to characterize the crystal phase. The field-emission scanning electron microscopy (FESEM, JEOL JSM 7800F) and transmission electron microscopy (TEM, JEOL JEM F200) were performed to display the microstructure. The X-ray photoelectron spectroscopy (XPS, Kratos AXIS SUPRA+) was conducted to investigate the chemical state. The Raman spectra (LabRAM HR Evolution) with a 532 nm laser were used to detect the material structure. Electron paramagnetic resonance (EPR, EMXnano) tests were used to confirm the defects. The N_2 adsorption-desorption tests (ASAP 2420) were implemented to measure the surface area and pore size. The ICP-OES test (Agilent 720ES) was performed to determine the content.

Electrochemical measurements:

The batteries were assembled by Swagelok-type shells (Fig. S1) for electrochemical tests. The electrolyte was composed of aluminum chloride and 1-ethyl-3-methylimidazolium chloride mixed with a molar ratio of 1.3:1. The active material, acetylene black, and polyvinylidene difluoride were mixed in N-methyl pyrrolidone solvent with a mass ratio of 8:1:1 to obtain the cathode slurry. The slurry was coated on the surface of molybdenum foil after stirring for 24 h and then dried in a vacuum at 60 ℃ for 12 h. The load mass of the cathode was about 1.2 mg cm^{-2}. The aluminum foil and glass-fiber membrane served as anode and separator, respectively. The galvanostatic charge/discharge tests

of batteries were performed by the Land CT2001A system in the voltage range of 0.01 to 2.0 V. The cyclic voltammetry (CV) and electrochemical impedance spectroscopy were tested by a CHI 660E electrochemical workstation. The Tafel tests were performed using symmetrical cells at a voltage range from –0.2 to 0.2 V with 1.0 mV s^{-1} by CHI 660E electrochemical workstation.

Theoretical calculations:

The first-principles computations were employed by the Vienna Ab initio Simulation Package based on Density Functional Theory. The exchange-correlation energy of electrons was described using generalized gradient approximation with the Perdew-Burke-Ernzerhof parametrization. The core-valence interaction was performed using the Projector Augmented Wave method. The cut-off energy was 320 eV and the *k-point* mesh was set to be 3×3×1. The energy convergence criteria were set to 10^{-5} eV.

Equation S1 for comparing Al^{3+} diffusion capability derived from the Randles–Sevcik equation.

$$I_{peak} = (2.69 \times 10^5)\, n^{1.5}\, S\, D_{Al3+}{}^{0.5}\, C_{Al}\, v^{0.5} \quad \textbf{S1}$$

where the I_{peak} is the peak current, n is the charge transfer number, S is the area of the cathode, D_{Al3+} is the Al^{3+} diffusion coefficient, C_{Al} is the concentration of Al^{3+} in the cathode, and v is the scan rate. The slope of the fitted curve (I_{peak} / $v^{0.5}$) represents the Al^{3+} diffusion rate as n, S, and C_{Al} are unchanged.

Equation S2 for evaluating capacitance-controlled and diffusion-controlled behaviors.

$$I\text{peak} = k_1 v + k_2 v^{1/2} \quad \textbf{S2}$$

where the ratio of k_1v and $k_2v^{1/2}$ refer to capacitance-controlled and diffusion-controlled behavior, respectively.

Equations S3 and **S4** for comparing electronic diffusion capability.

$$D = \frac{R^2T^2}{2A^2n^4F^4C^2\sigma^2} \quad \textbf{S3}$$

$$Z` = R_{ct} + R_e\sigma\omega^{-1/2} \quad \textbf{S4}$$

where the R, T, A, n, F, C, δ refer to the gas constant, absolute temperature, area of the cathode, charge transfer number, Faraday constant, concentration of Al^{3+}, and Warburg factor, respectively. The slope of the fitted curve (Z' / $\omega^{-1/2}$) mainly determines the diffusion coefficient (D) as other parameters are unchanged.

Equation S5 for calculating the Al^{3+} diffusion coefficient according to the GITT results.

$$D\text{Al3} + = \frac{4}{\pi\tau}\left(\frac{m_bV_m}{M_bS}\right)^2\left(\frac{\Delta E_s}{\Delta E_\tau}\right)^2 \quad \textbf{S5}$$

where the τ, m_b, V_m, M_b, and S represent relaxation time, mass, molar volume, molar mass, and area of the cathode, respectively. The ΔE_s and ΔE_τ are voltage variations occurring in relaxation steps and the current pulse.

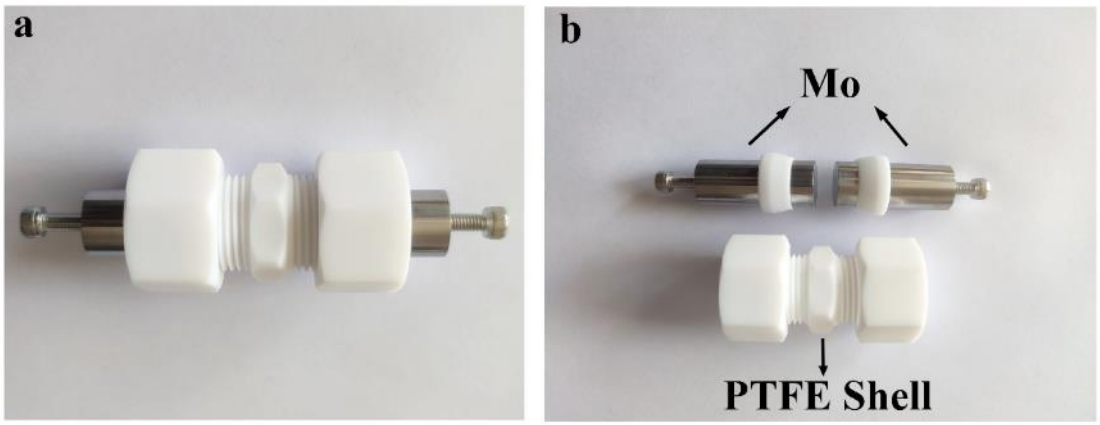

Fig. S1 Digital images of (a) Swagelok-type shell and (b) corresponding disassembled parts.

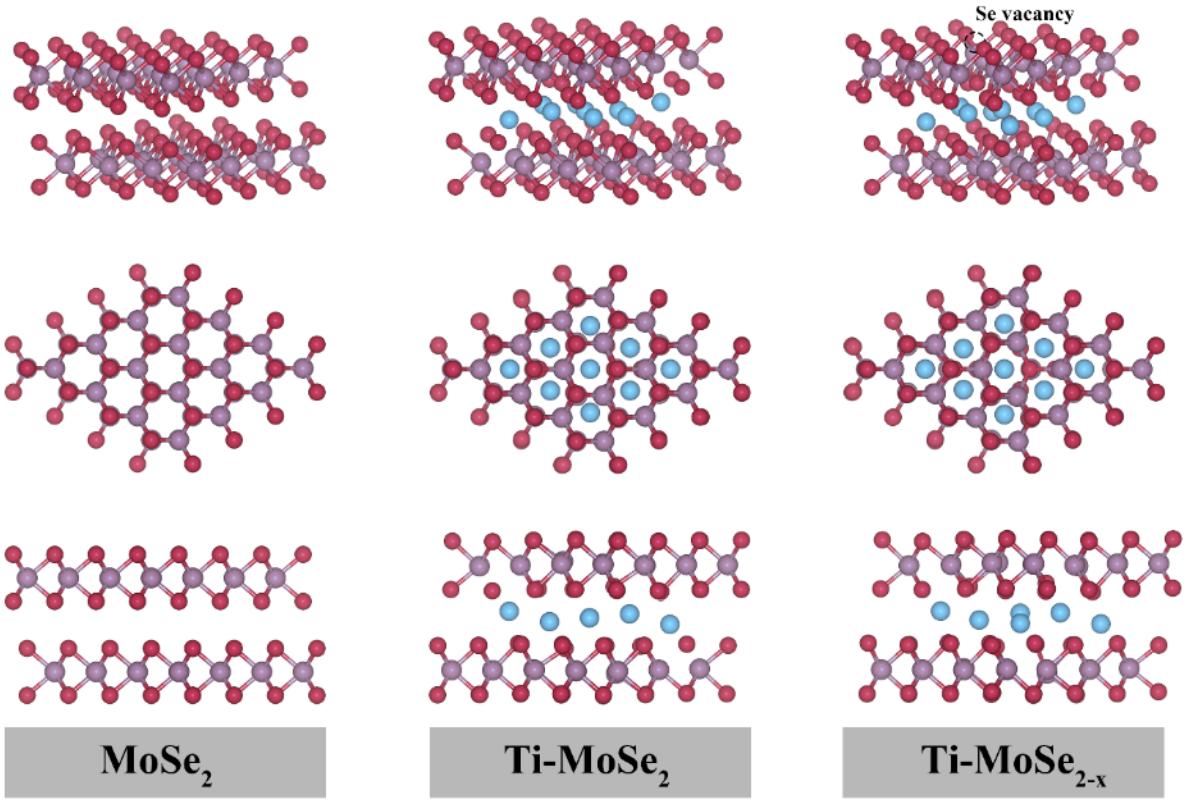

Fig. S2 Optimized structural models of $MoSe_2$, Ti-$MoSe_2$, and Ti-$MoSe_{2-x}$.

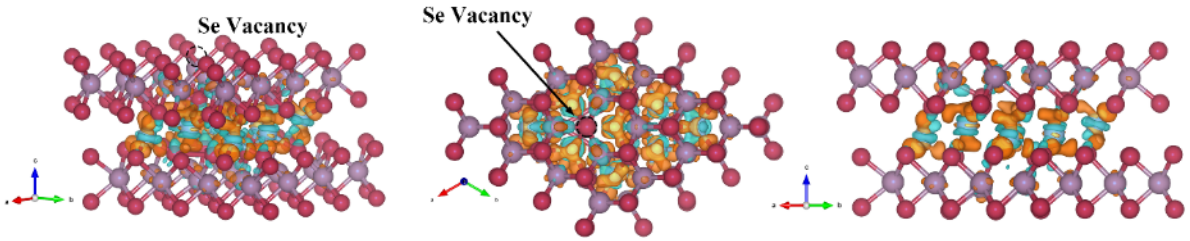

Fig. S3 Charge density difference of Ti-$MoSe_{2-x}$. The orange and blue regions represent charge accumulation and delocalization, respectively.

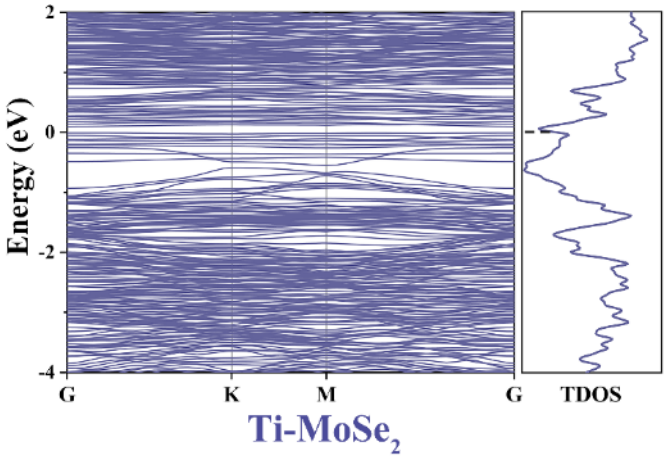

Fig. S4 Energy band structure of Ti-$MoSe_2$,

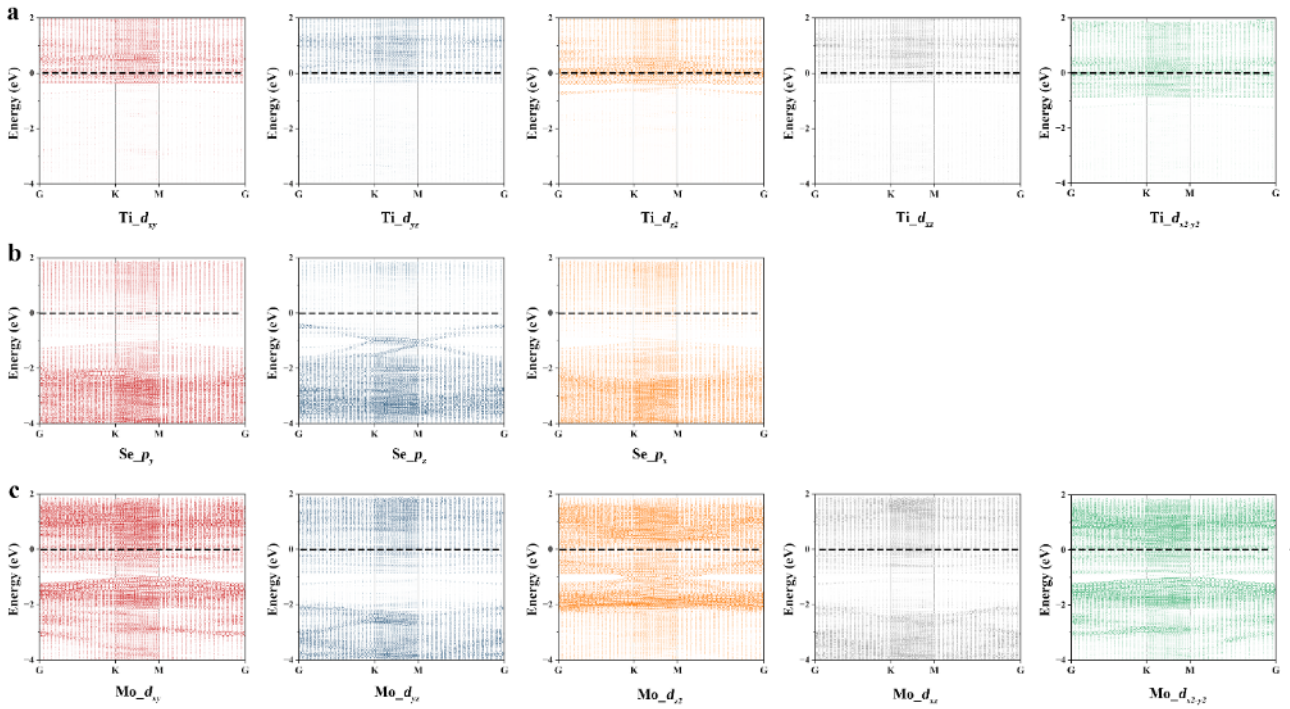

Fig. S5 Projected band of (a) Ti_3*d*, (b) Se_4*p*, and (c) Mo_4*d* orbits in Ti-$MoSe_{2-x}$.

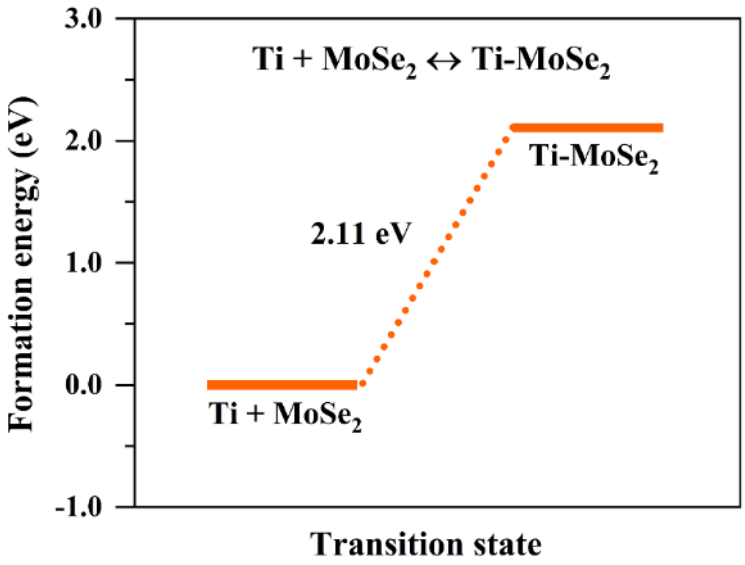

Fig. S6 Formation energy of Ti-$MoSe_2$.

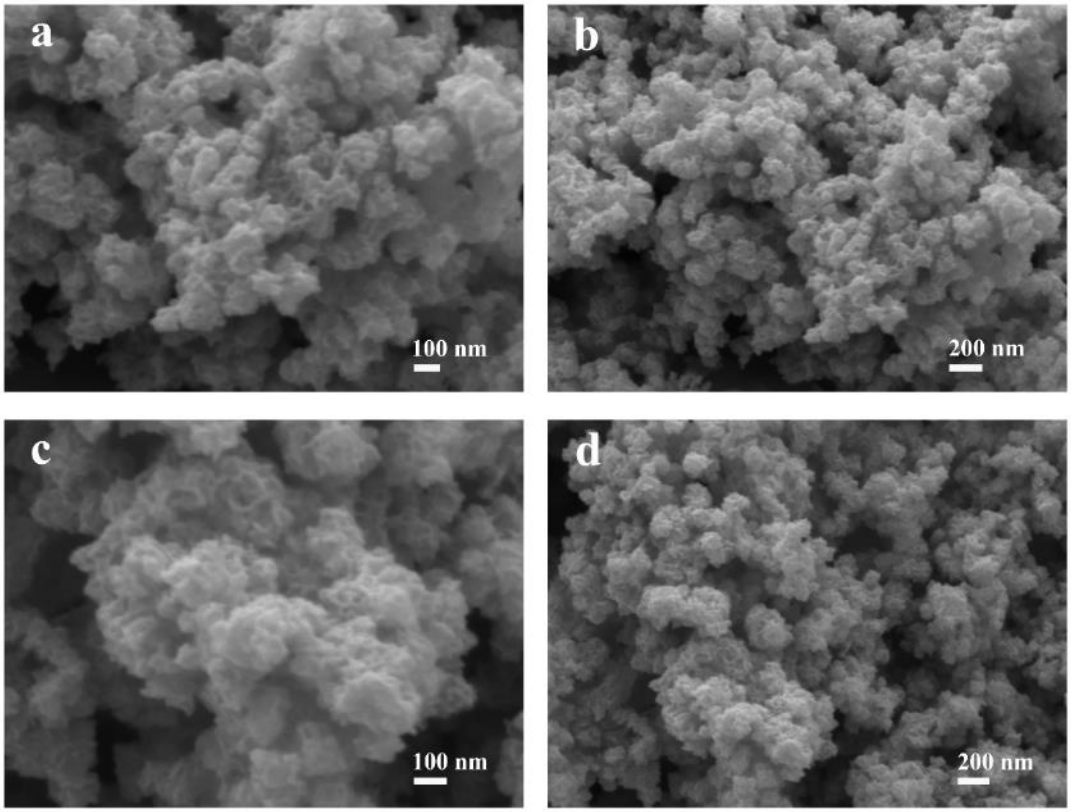

Fig. S7 FESEM images of $MoSe_2$.

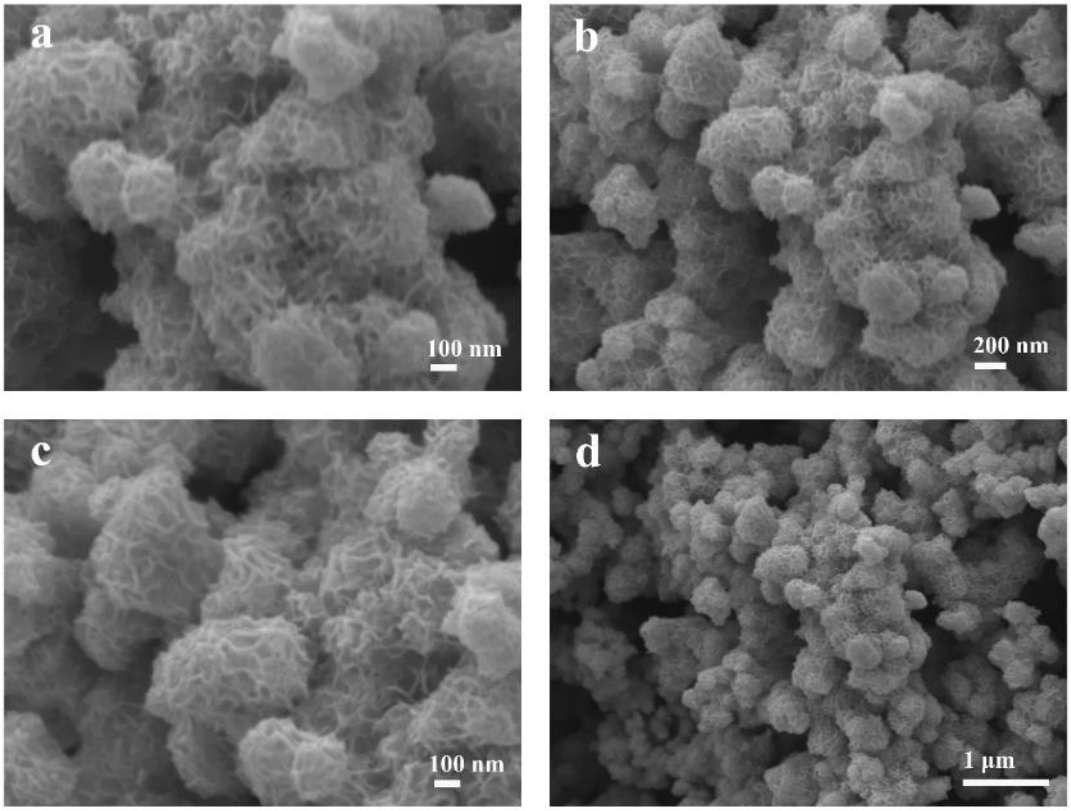

Fig. S8 FESEM images of Ti-$MoSe_2$.

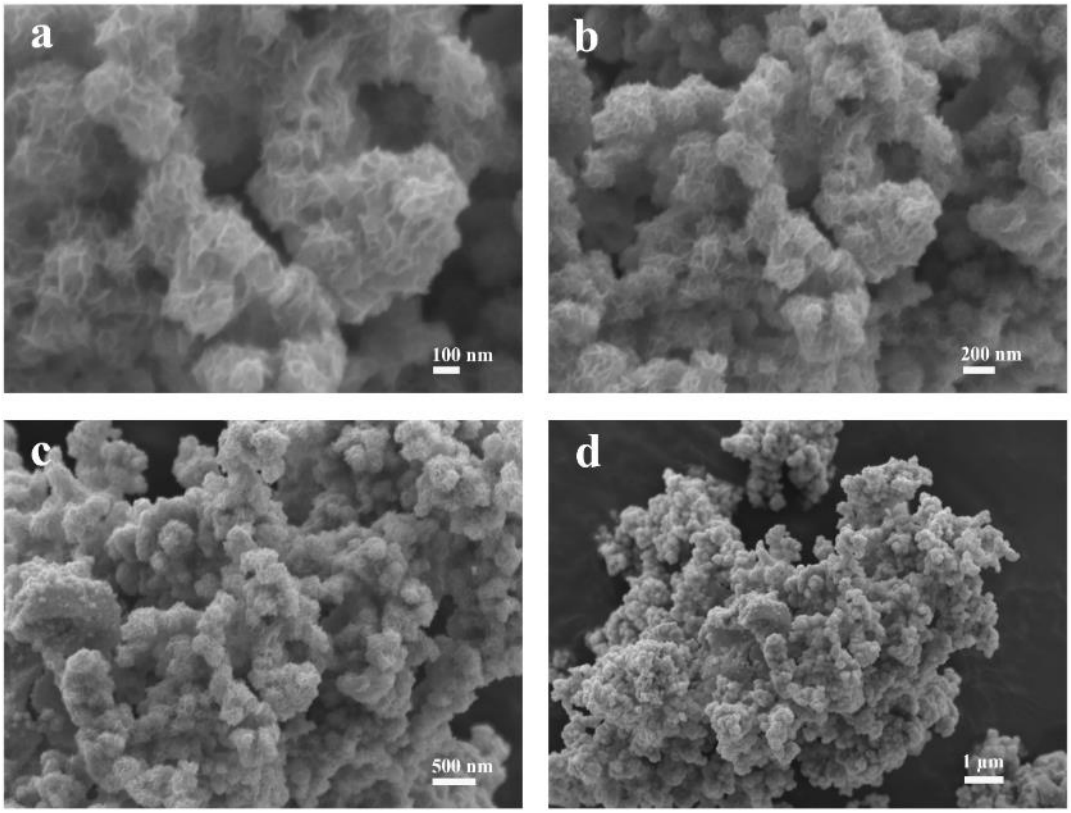

Fig. S9 FESEM images of Ti-$MoSe_{2-x}$.

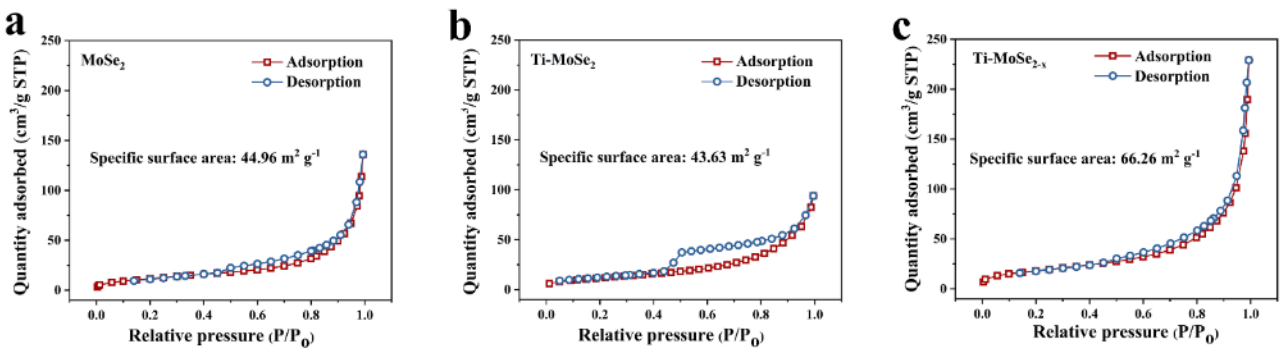

Fig. S10 Nitrogen adsorption/desorption isotherms of (a) $MoSe_2$, (b) Ti-$MoSe_2$, and (c) Ti-$MoSe_{2-x}$.

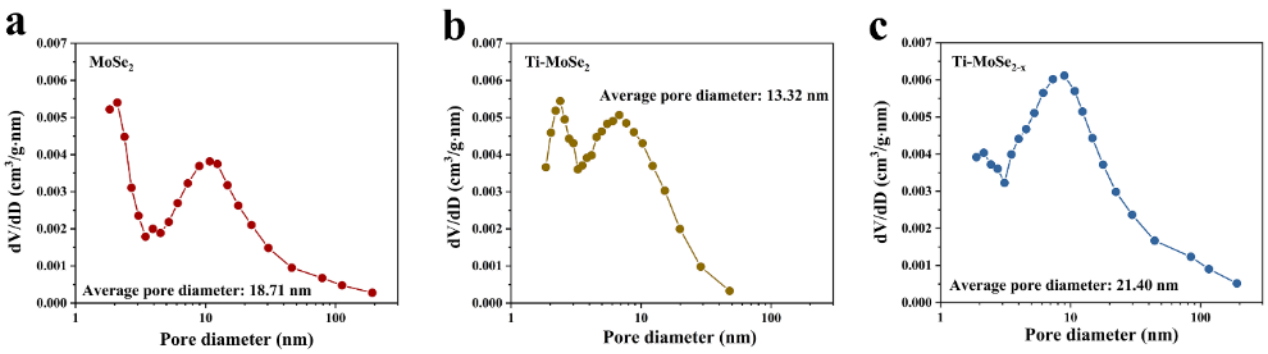

Fig. S11 Pore size distribution curves of (a) $MoSe_2$, (b) Ti-$MoSe_2$, and (c) Ti-$MoSe_{2-x}$.

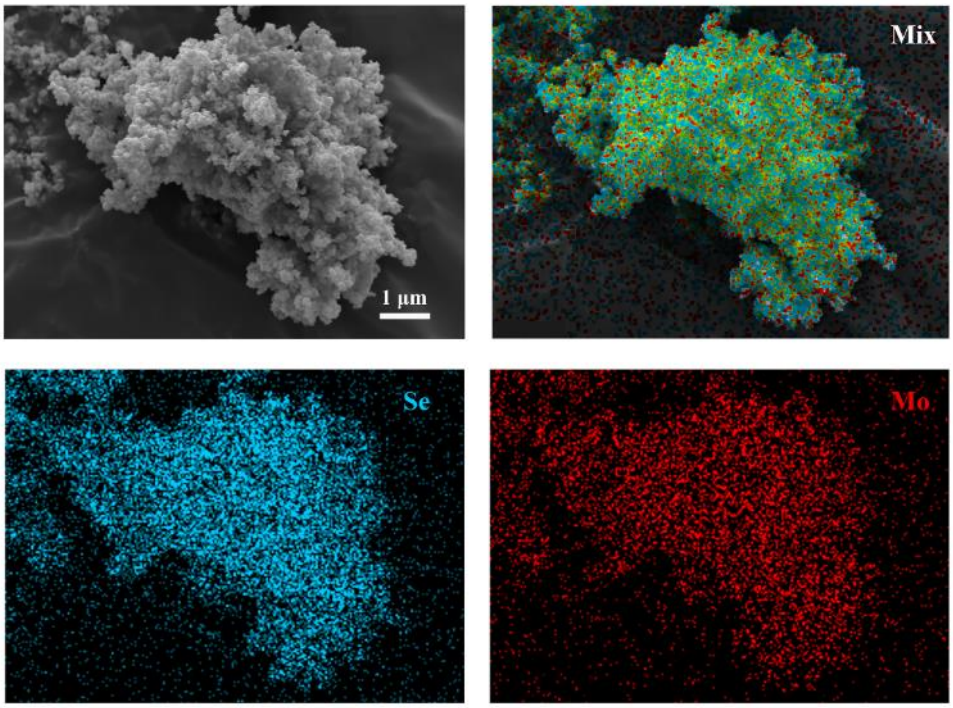

Fig. S12 EDX mappings of $MoSe_2$.

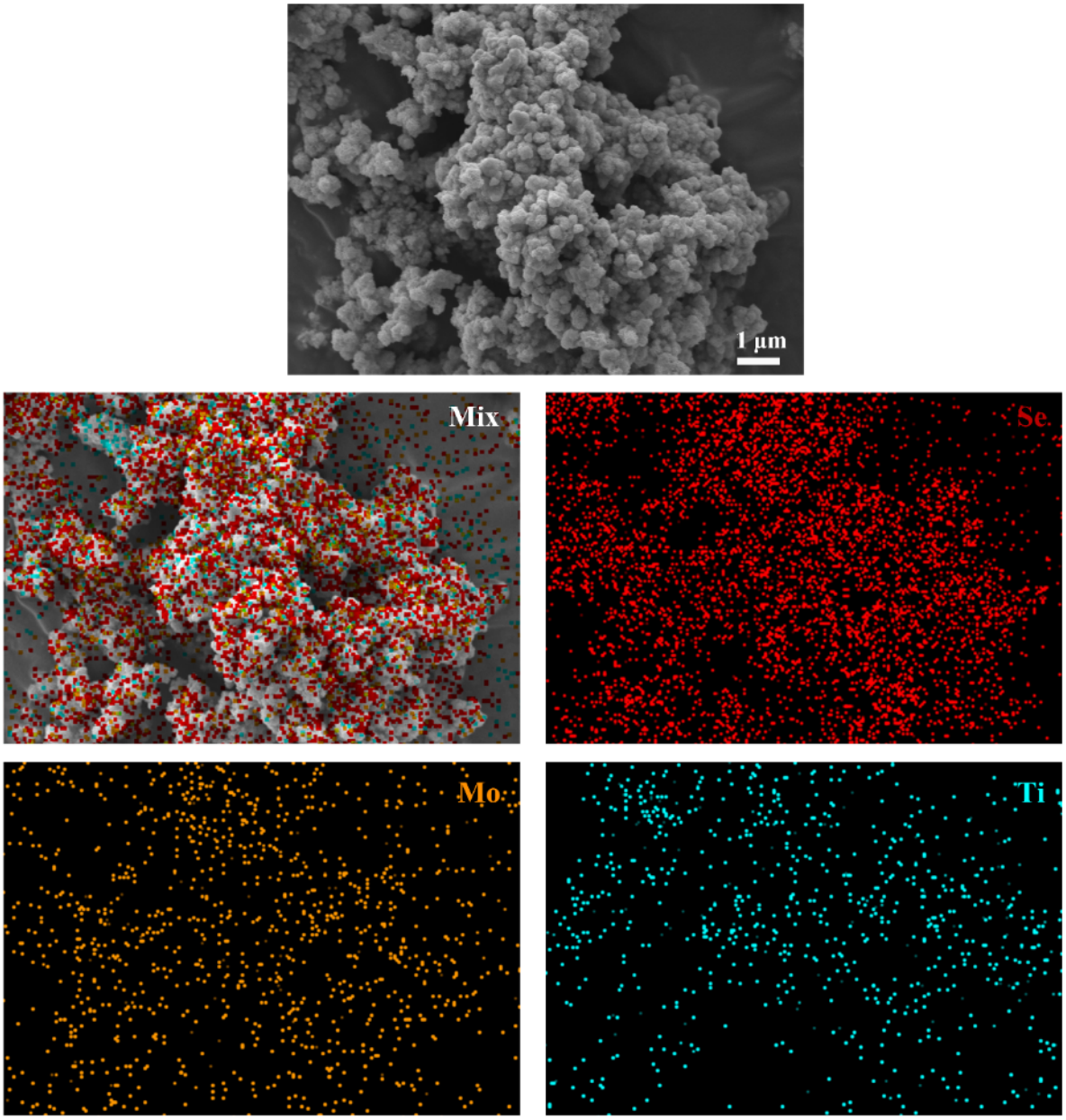

Fig. S13 EDX mappings of Ti-$MoSe_2$.

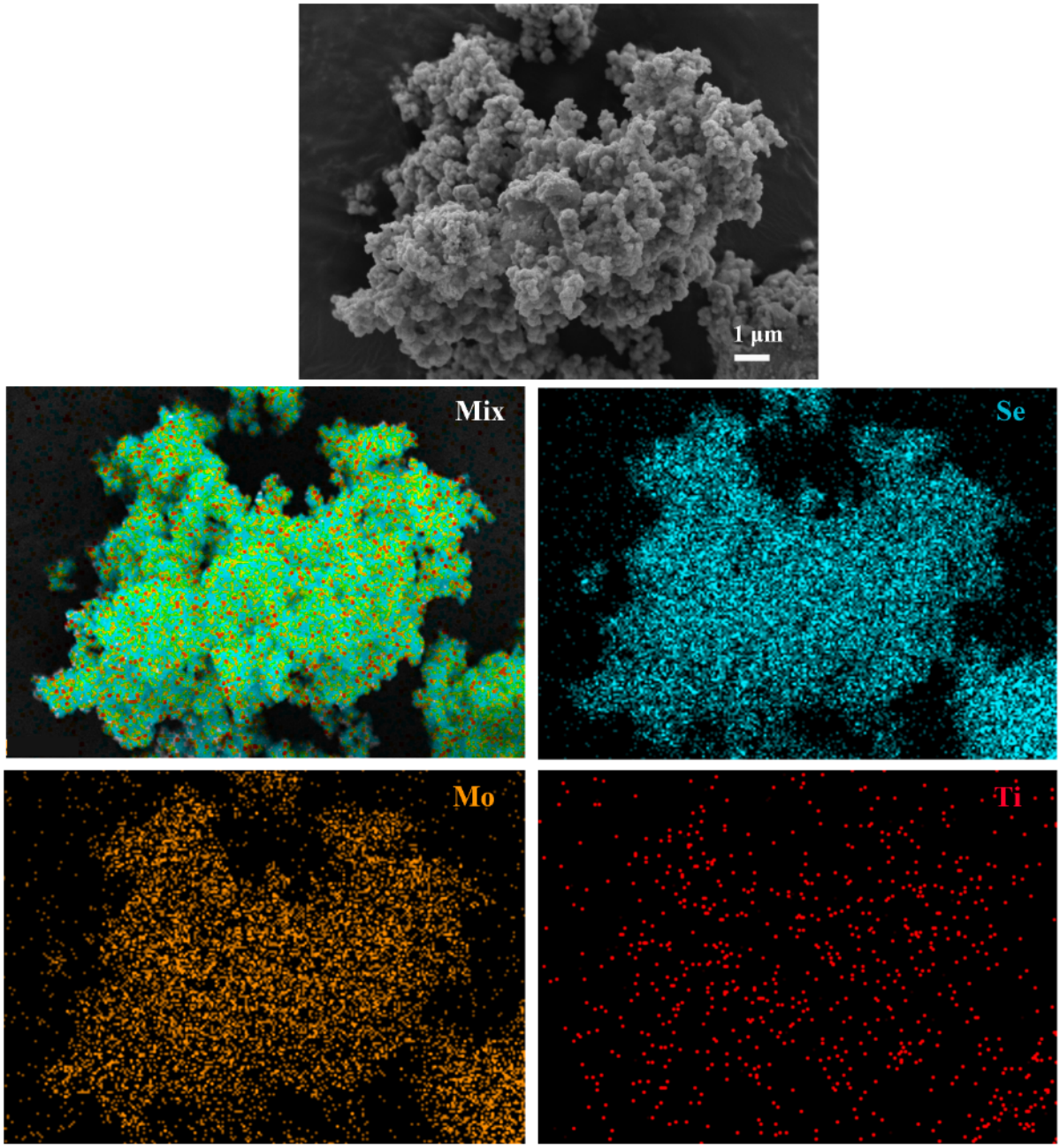

Fig. S14 EDX mappings of Ti-$MoSe_{2-x}$.

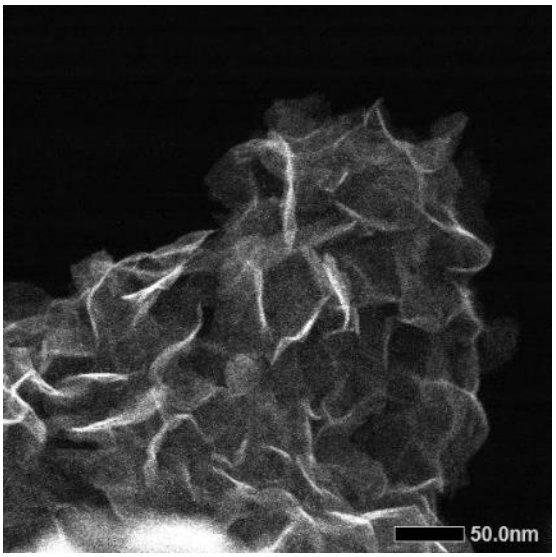

Fig. S15 STEM image of Ti-$MoSe_{2-x}$.

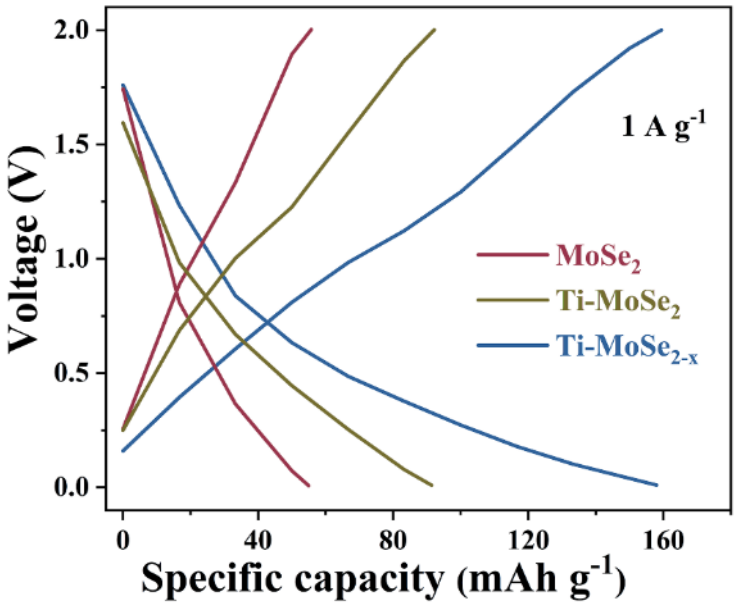

Fig. S16 Charge/discharge profiles at 1.0 A g^{-1}.

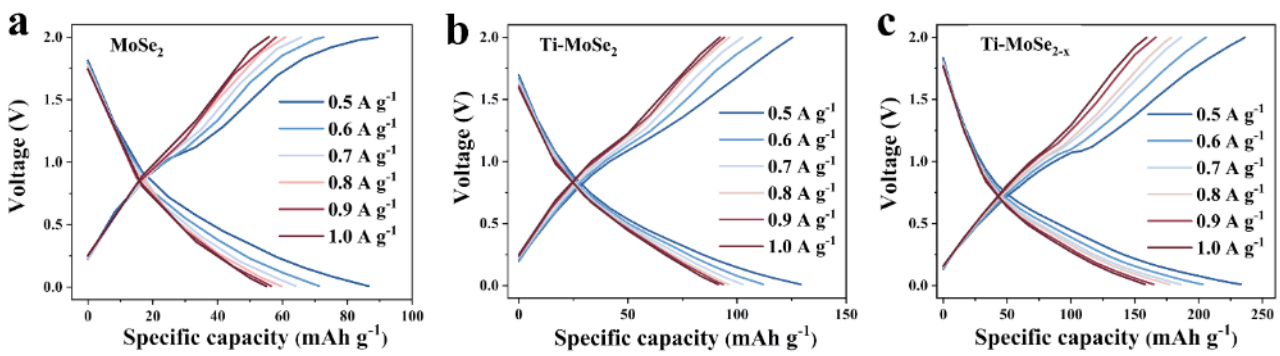

Fig. S17 Charge/discharge profiles of (a) $MoSe_2$, (b) Ti-$MoSe_2$, and (c) Ti-$MoSe_{2-x}$ cathodes at current densities from 0.5 to 1.0 A g^{-1}.

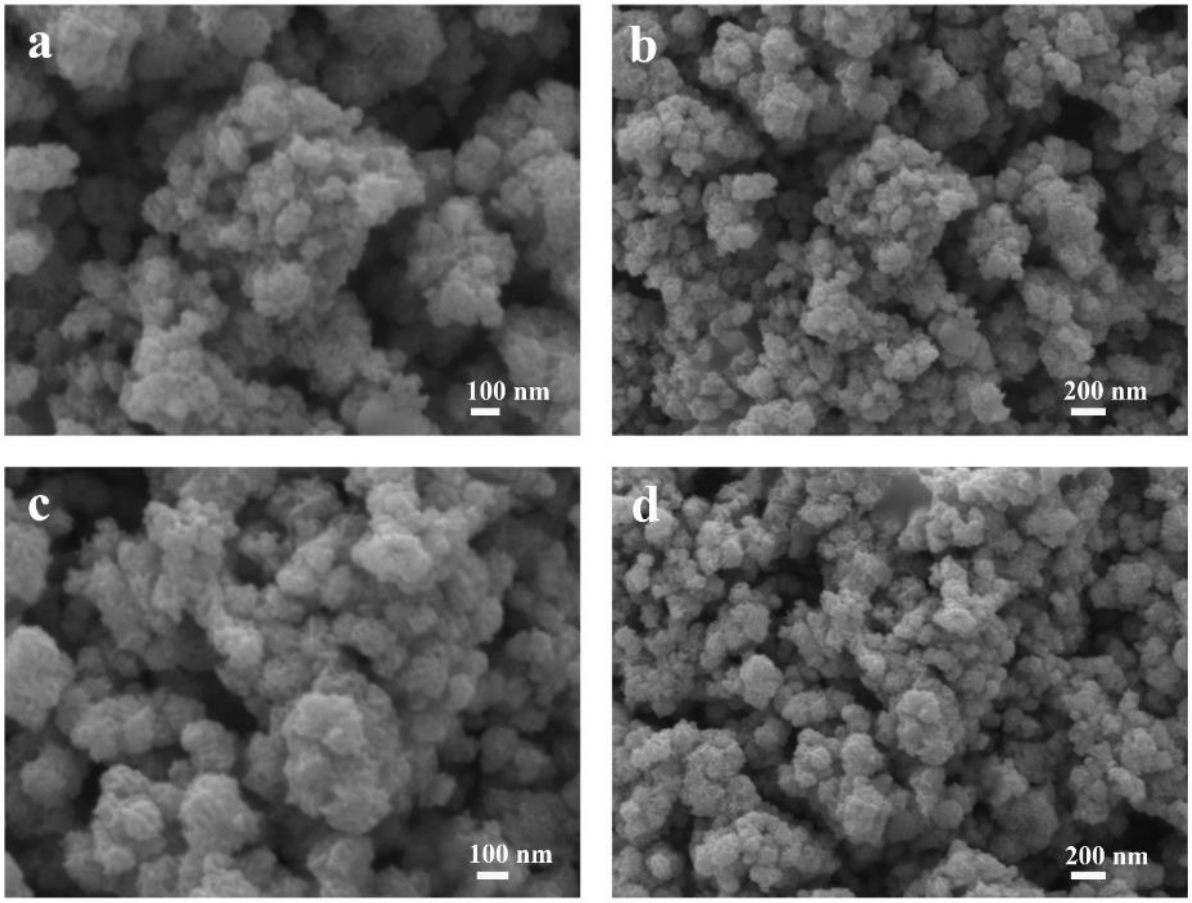

Fig. S18 FESEM images of $MoSe_{2-x}$.

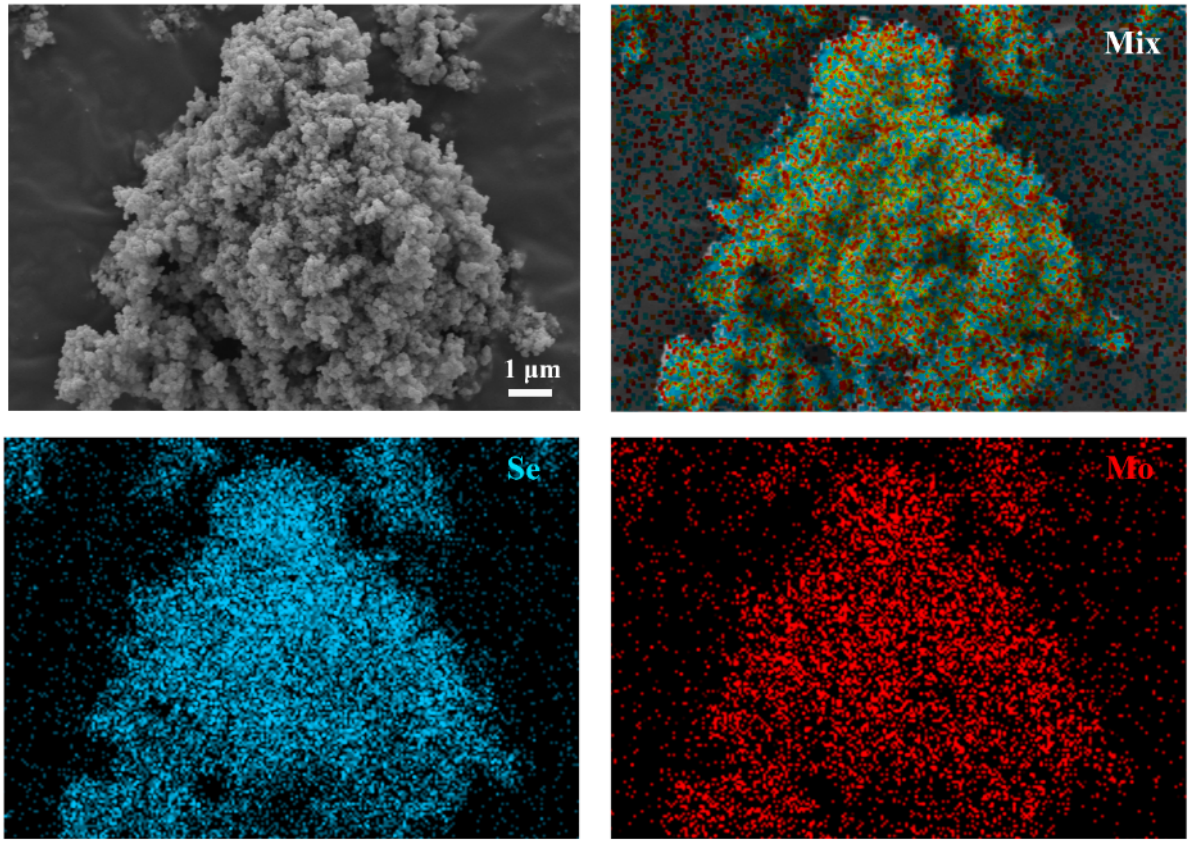

Fig. S19 EDX mappings of $MoSe_{2-x}$.

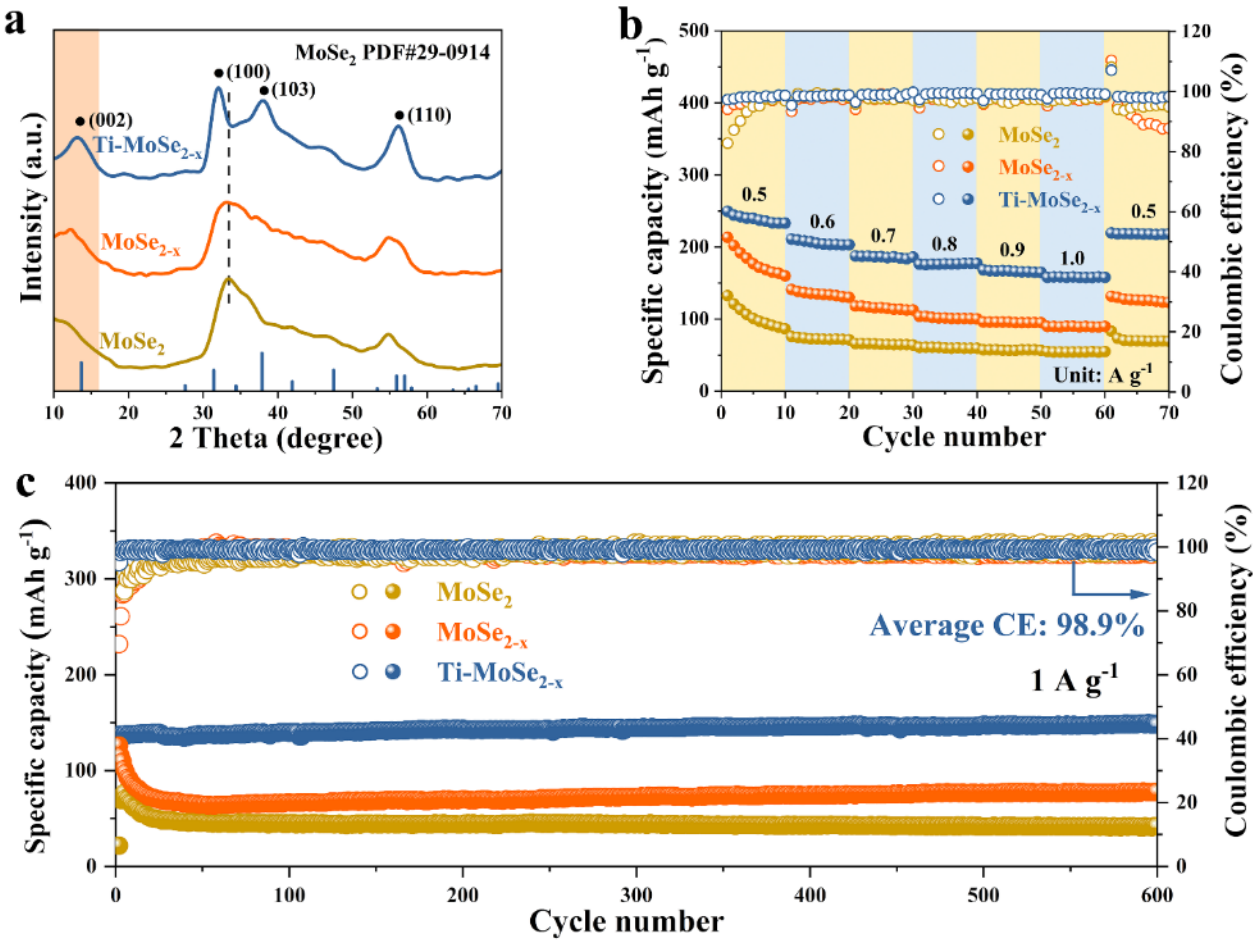

Fig. S20 (a) XRD patterns, (b) rate capacity, and (c) cycling stability of $MoSe_2$, $MoSe_{2-x}$, and Ti-$MoSe_{2-x}$.

According to the FESEM images (Fig. S18), the $MoSe_{2-x}$ appears as nanoparticles with a rough surface, and the diameters are predominantly distributed between 100–150 nm. The morphology of $MoSe_{2-x}$ is similar to that of $MoSe_2$, indicating that the microwave process has little effect on the morphology. The EDX mappings (Fig. S19) of $MoSe_{2-x}$ demonstrate a uniform distribution of Mo and Se elements.

In the XRD pattern (Fig. S20a) of $MoSe_{2-x}$, a slight shift towards a lower angle is observed for the (100) characteristic peak, and the (002) peak is intensified compared to the pristine $MoSe_2$. This could be attributed to lattice distortion and an increase in layer spacing caused by the microwave process. Moreover, the electrochemical performance of $MoSe_{2-x}$ has been tested and presented in Fig. S20b,c. In the rate performance tests, the $MoSe_{2-x}$ displays specific capacities of 160 (10^{th}), 130 (20^{th}), 113 (30^{th}), 100 (40^{th}), 95 (50^{th}), and 90 (60^{th}) mAh g^{-1} at 0.5, 0.6, 0.7, 0.8, 0.9, and 1.0 A g^{-1}, respectively. Compared to the pristine $MoSe_2$, the $MoSe_{2-x}$ exhibits a significant enhancement in

capacity, yet it still suffers from severe capacity decay. In the cycling stability tests at 1.0 A g^{-1}, despite the $MoSe_{2-x}$ demonstrating a high initial capacity of 126 mAh g^{-1}, the retention rate after 600 cycles is only 61%. Similar to $MoSe_2$, the $MoSe_{2-x}$ is observed to possess a drastic capacity decline within the first 30 cycles. The performance of $MoSe_{2-x}$ can be summarized as having an increased capacity but still with an unstable structure. In contrast, the electrochemical performance of Ti-$MoSe_2$ (Fig. 3 and Fig. 4) shows high cycling stability and electron conductivity.

Therefore, according to the characterizations of $MoSe_2$, $MoSe_{2-x}$, Ti-$MoSe_2$, and Ti-$MoSe_{2-x}$, it can be deduced that the Ti element primarily enhances structural stability and electron conductivity as interlayer pillars, while the SVs mainly increase specific capacity by acting as additional active sites. Owing to the synergistic effects of Ti intercalation and SVs, the Ti-$MoSe_{2-x}$ exhibits outstanding and comprehensive electrochemical performance.

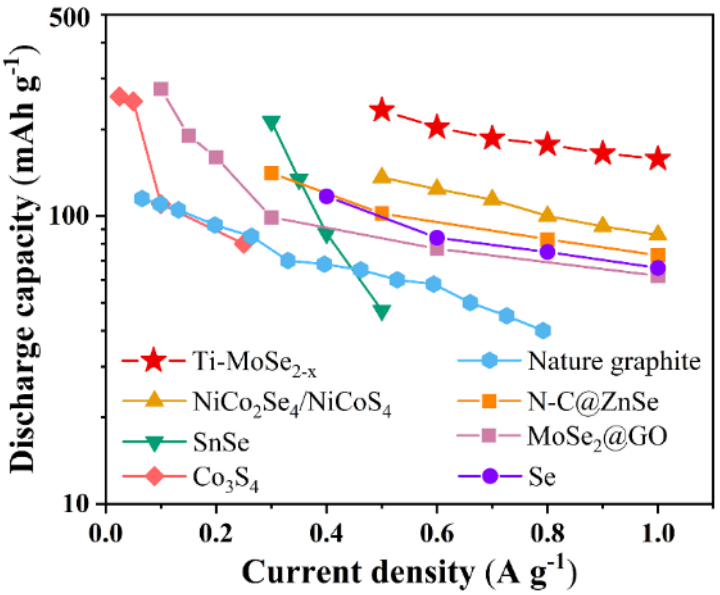

Fig. S21 Comparison of rate performance between Ti-$MoSe_{2-x}$ and reported cathodes in ABs.

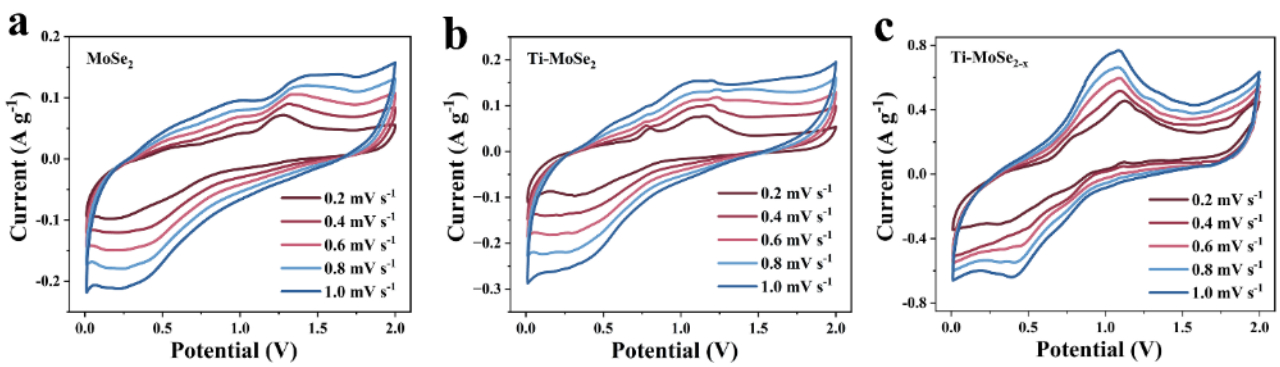

Fig. S22 CV curves of (a) $MoSe_2$, (b) Ti-$MoSe_2$, and (c) Ti-$MoSe_{2-x}$ cathodes at scan rates from 0.2 to 1.0 mV s^{-1}.

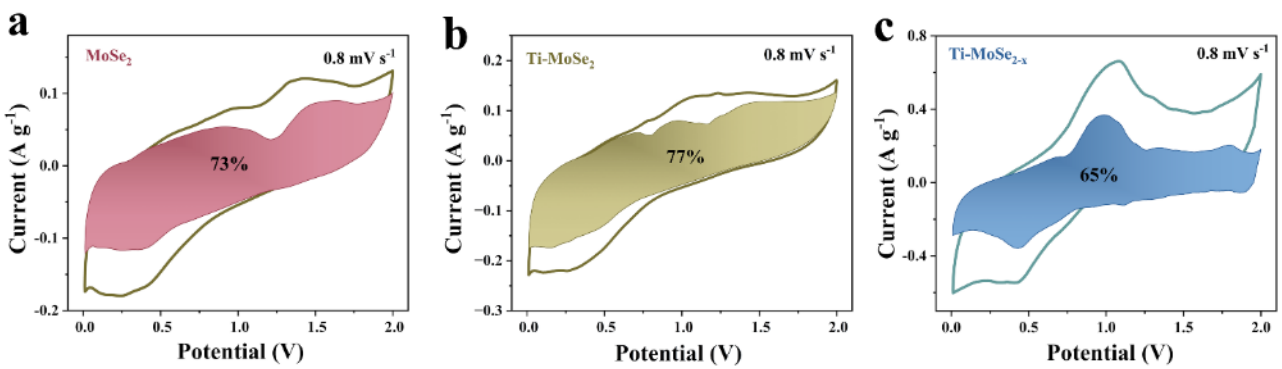

Fig. S23 Capacitive contribution of (a) $MoSe_2$, (b) Ti-$MoSe_2$, and (c) Ti-$MoSe_{2-x}$ cathodes at a scan rate of 0.8 mV s^{-1}.

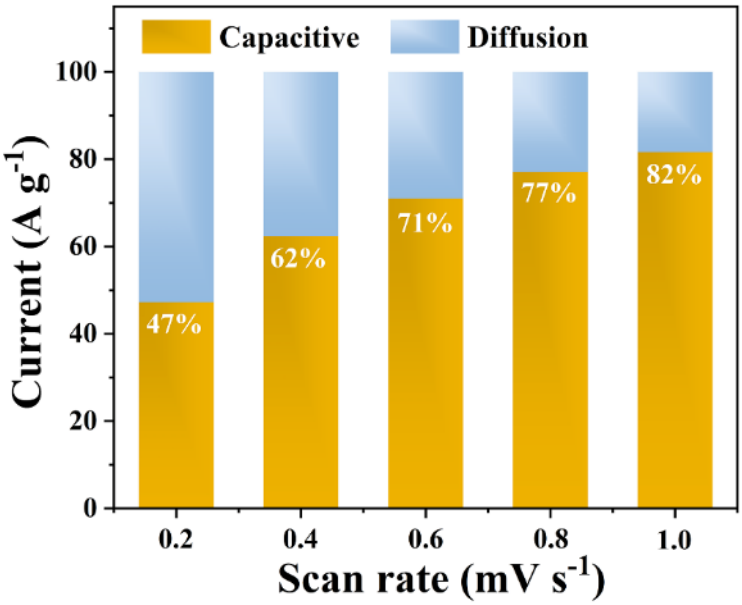

Fig. S24 Capacitive contributions of Ti-$MoSe_2$ at scan rates from 0.2 to 1.0 mV s^{-1}.

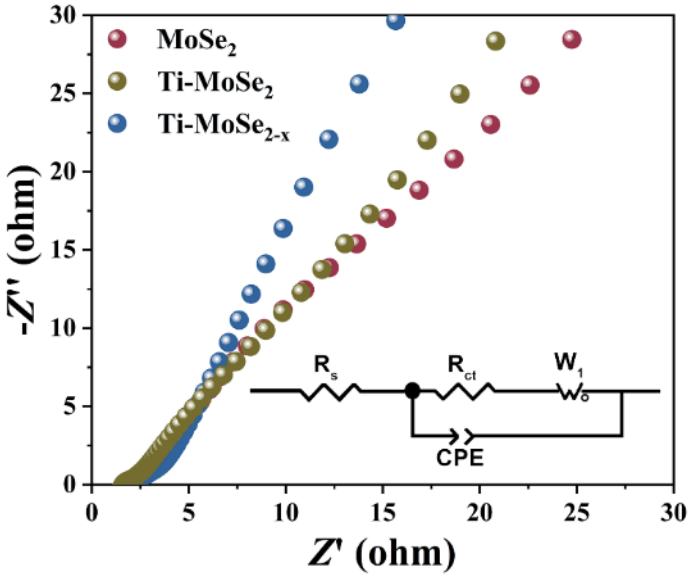

Fig. S25 Nyquist plots of $MoSe_2$, Ti-$MoSe_2$, and Ti-$MoSe_{2-x}$ cathodes.

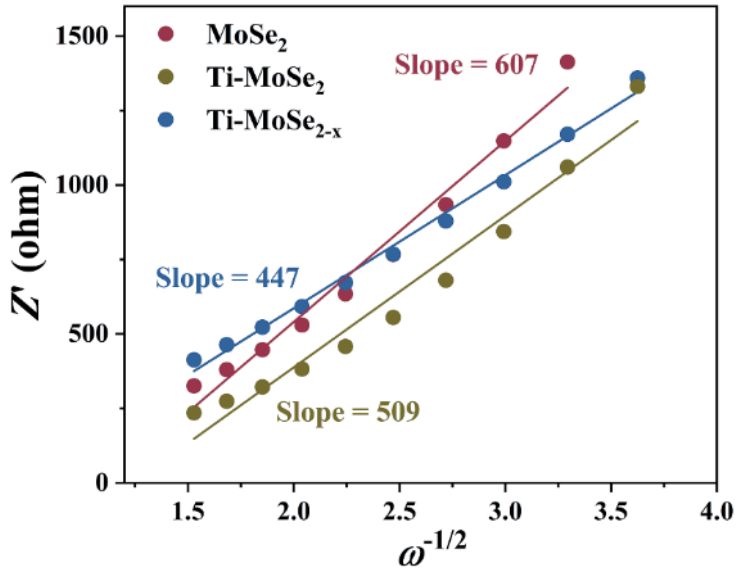

Fig. S26 Fitted plots of $Z`$ and $\omega^{-1/2}$ for evaluating electronic diffusion capability.

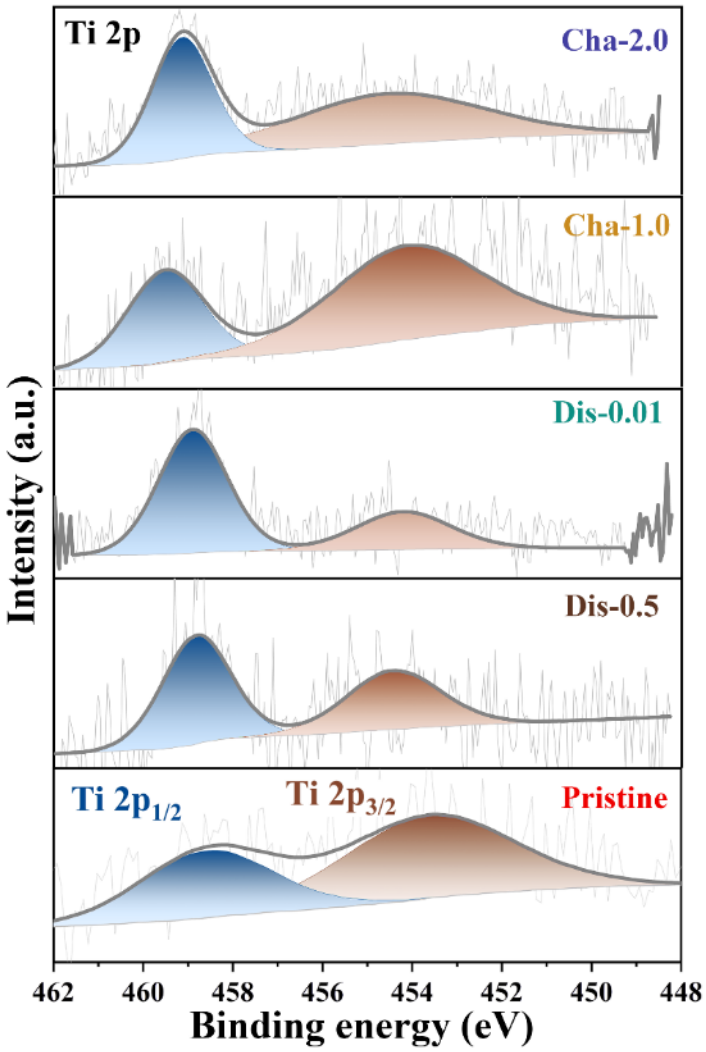

Fig. S27 Ex situ XPS spectrum of Ti 2*p*.

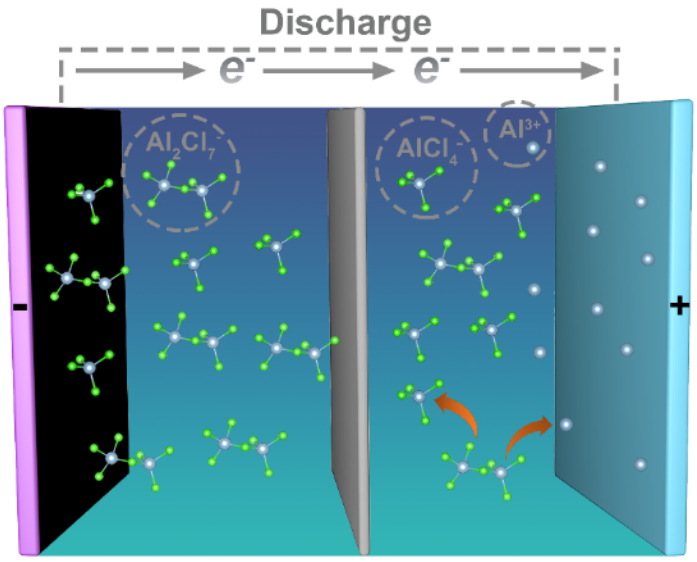

Fig. S28 Schematic diagram of the energy-storage mechanism of Ti-$MoSe_{2-x}$ cathode in ABs.

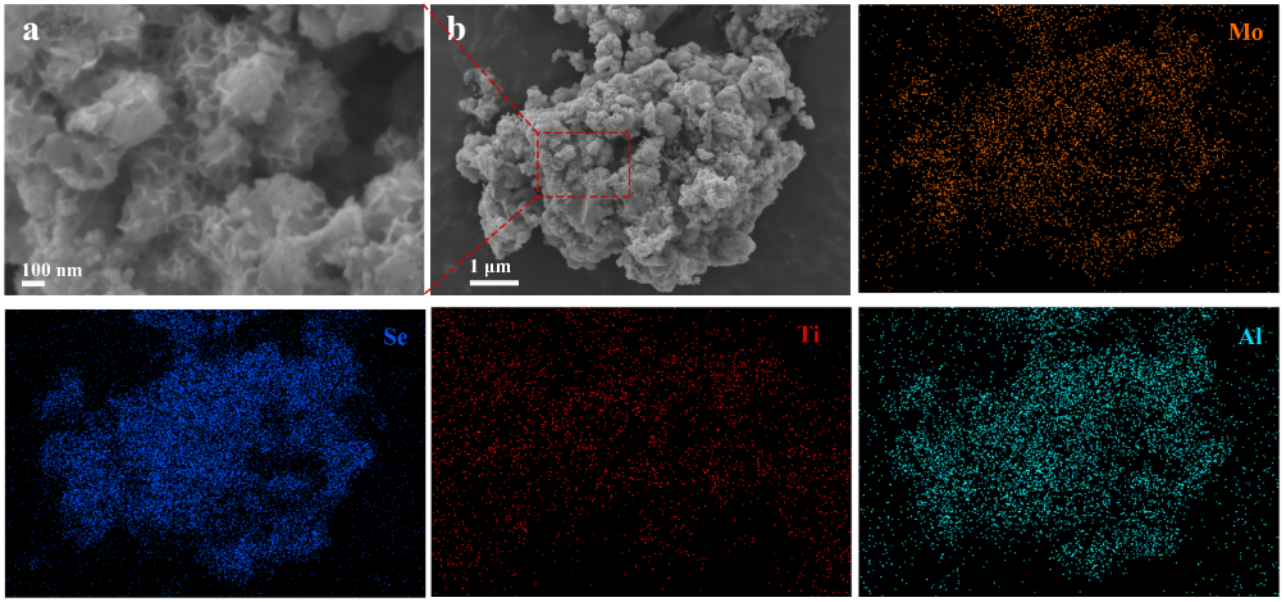

Fig. S29 (a) FESEM image and (b) EDX mappings of the Ti-$MoSe_{2-x}$ cathode after 100 charged/diacharged cycles.

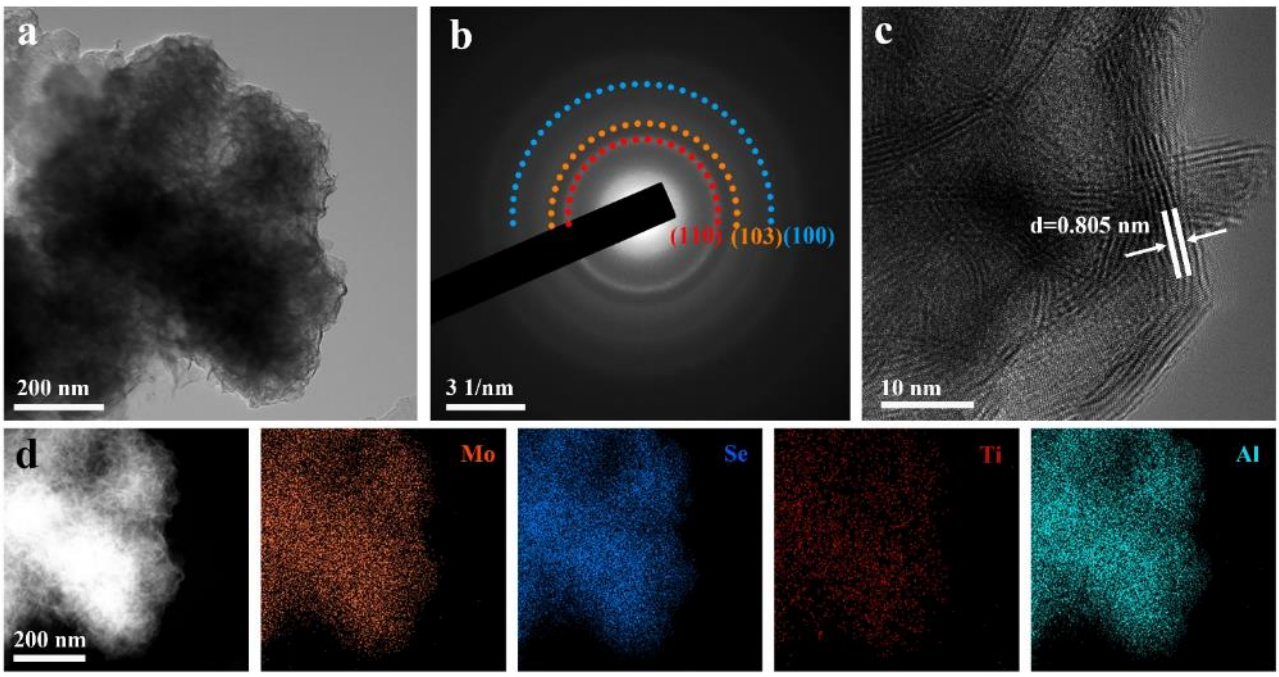

Fig. S30 (a) TEM image, (b) SAED pattern, (c) HRTEM image, and (d) EDX mappings of the Ti-$MoSe_{2-x}$ cathode after 100 charged/diacharged cycles.

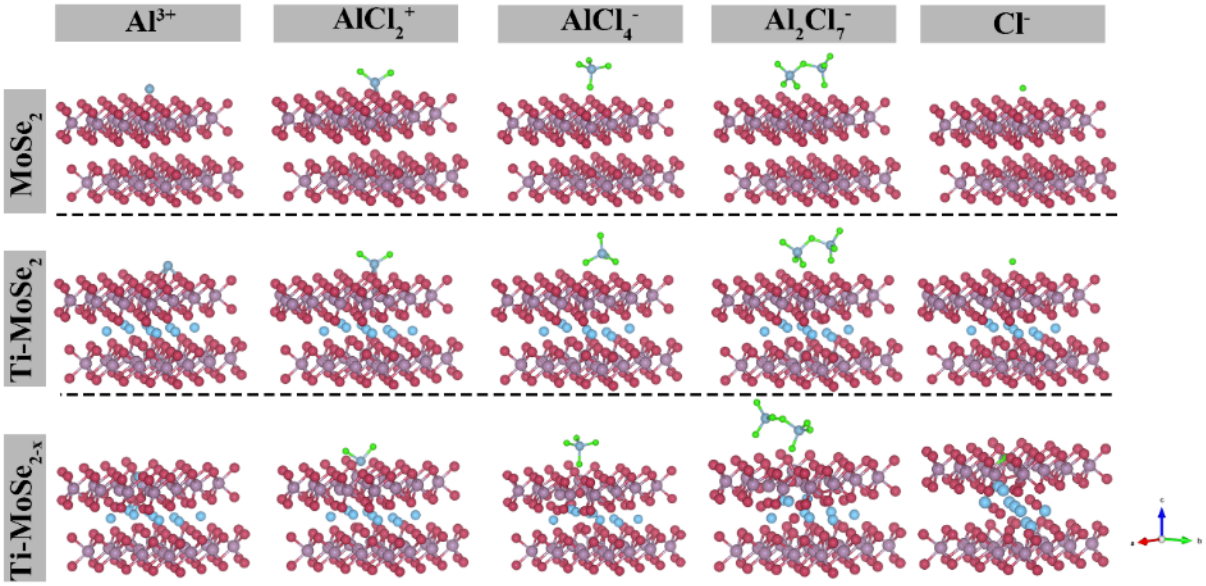

Fig. S31 Structural models of $MoSe_2$, Ti-$MoSe_2$, and Ti-$MoSe_{2-x}$ adsorbing active species.

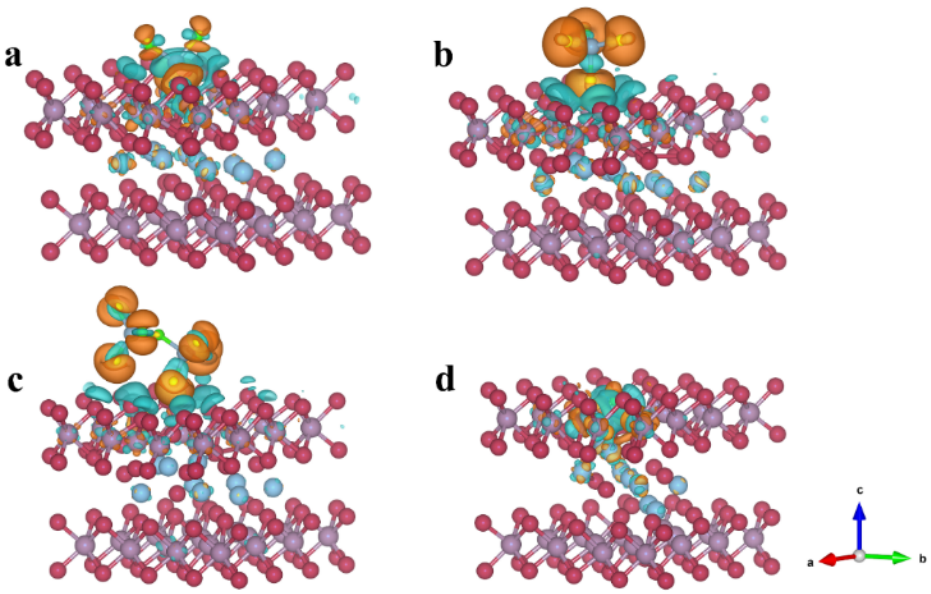

Fig. S32 Charge density differences of Ti-$MoSe_{2-x}$ adsorbing (a) $AlCl_2^+$, (b) $AlCl_4^-$, (c) $Al_2Cl_7^-$, and (d) Cl^-.

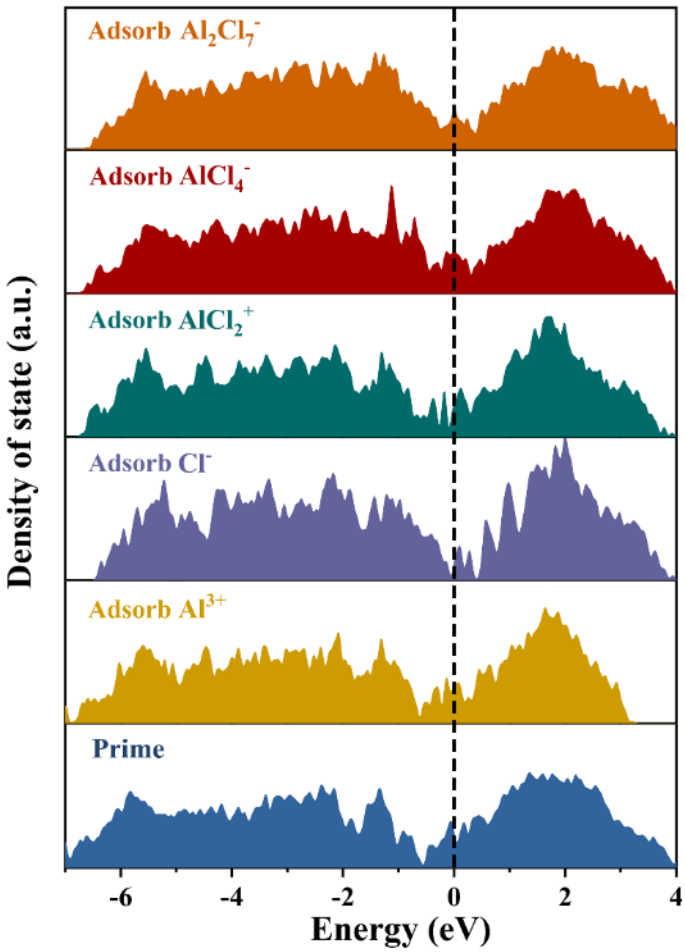

Fig. S33 DOS of Ti-$MoSe_{2-x}$ adsorbing electrolyte ions.

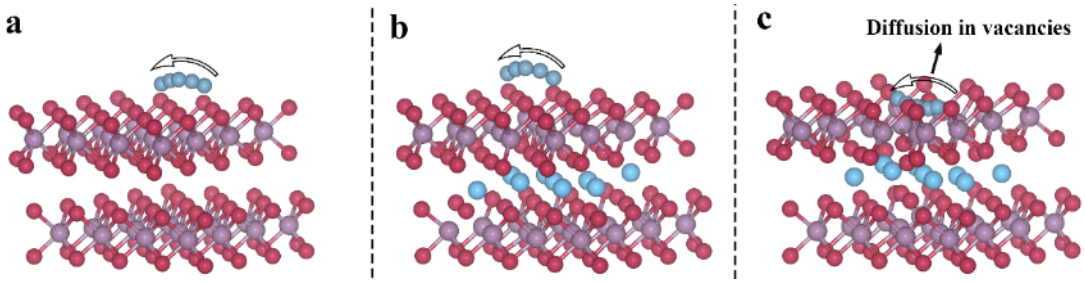

Fig. S34 Migration pathways of Al^{3+} on (a) $MoSe_2$, (b) Ti-$MoSe_2$, and (c) Ti-$MoSe_{2-x}$.

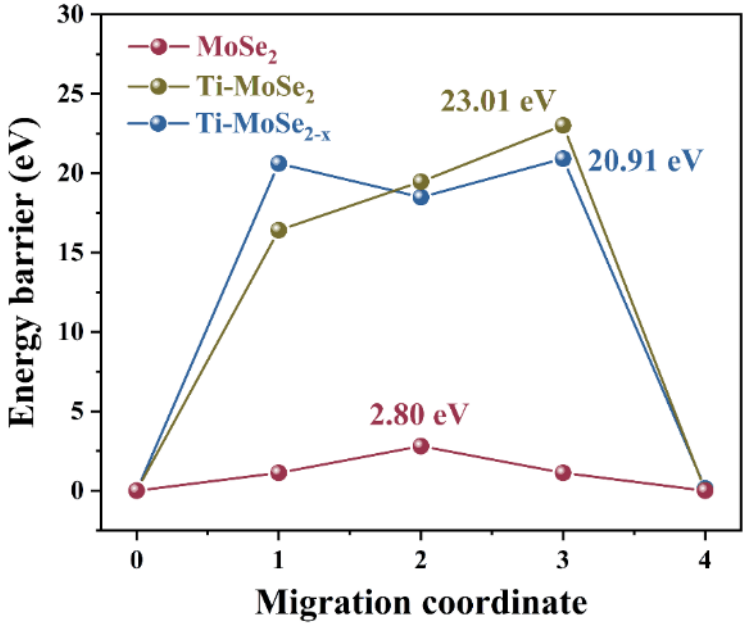

Fig. S35 Migration energy barriers of Al^{3+} between layers.

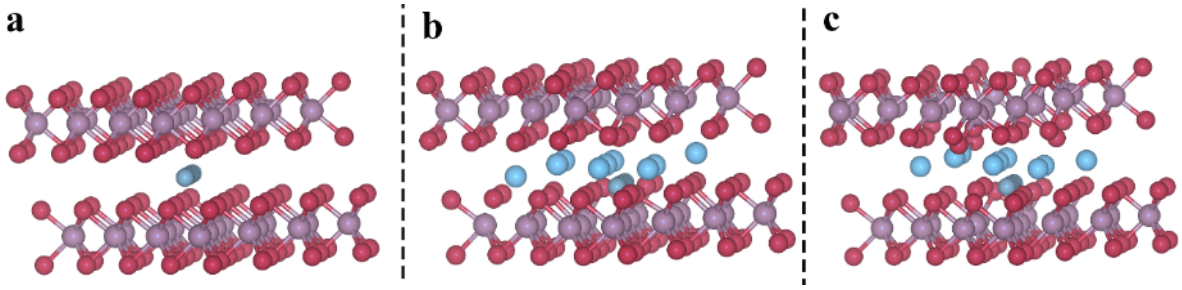

Fig. S36 Migration pathways of Al^{3+} in (a) $MoSe_2$, (b) Ti-$MoSe_2$, and (c) Ti-$MoSe_{2-x}$.

Table S1 ICP-OES results for Ti-$MoSe_{2-x}$.

Mo	Se	Ti
36.89 wt%	60.83 wt%	0.74 wt%

Table S2 Comparison of electrochemical performance between Ti-$MoSe_{2-x}$ and reported cathodes.

Strategy	Capacity (mAh g^{-1})	Cycle (number)	Current density (A g^{-1})	Reference
Ti-$MoSe_{2-x}$	**148** **136**	**600** **2400**	**1** **5**	**This work**
CNS@MC	167	350	1	[*Adv. Funct. Mater.* **2024**, 34, 2315603]
Expanded graphite	144	100	0.1	[*Carbon* **2024**, 223, 119016]
PVBPX	133	100	0.2	[*Angew. Chem.* **2023**, 135, e202216797]
SPANI	165	300	0.1	[*Adv. Mater.* **2022**, 34, 2106511]
FeF_3@EG	80	150	0.1	[*Adv. Energy Mater.* **2022**, 12, 2200959]
Li–VONB	162	300	0.05	[*Adv. Energy Mater.* **2022**, 12, 2201653]
Nb_2CTx	80	500	0.5	[*ACS Appl. Mater. Interfaces* **2022**, 14, 45254]
Activated carbon	80	1500	1	[*Carbon* **2022**, 191, 195]
$Al_{2/3}Li_{1/3}Mn_2O_4$	93	1000	1	[*Energy Storage Mater.* **2022**, 53, 514]
V_2C@Se	119	1000	1	[*Energy Storage Mater.* **2022**, 46, 138]
$CoSe_2$	148	500	0.5	[*Chem. Eng. J.* **2022**, 430, 133135]
Ti_3C_2	134	500	0.5	[*J. Energy Chem.* **2022**, 74, 174]
$(Fe,Mn,Ni,Zn,Mg)_3O_4$	163	200	1	[*Small* **2023**, 20, 2305998]
S-MoS_2	129	1000	1	[*J. Mater. Chem. A* **2023**,11, 15509]
Co_3Se_4/ZnSe	117	500	0.2	[*ACS Appl. Mater. Interfaces* **2023**, 15, 11906]
C4Q	102	500	0.2	[*J. Mater. Chem. A* **2023**,11, 13527]
Co_3Sn_2@GO	114	100	0.2	[*Small* **2022**, 18, 2203236]
S-WSe_2	110	1500	2	[*Small Methods* **2022**, 6, 2201281]
Bi_2Te_3/Sb_2Te_3	101	3000	5	[*Energy Storage Mater.* **2021**, 38, 231]

Table S3 Adsorption energies of active species on $MoSe_2$, Ti-$MoSe_2$, and Ti-$MoSe_{2-x}$.

Systems	Al^{3+}	$AlCl_2^+$	$AlCl_4^-$	$Al_2Cl_7^-$	Cl^-
$MoSe_2$	–1.34	–1.06	–1.21	–1.66	–1.20
Ti-$MoSe_2$	–2.01	–1.71	–2.44	–1.50	–2.13
Ti-$MoSe_{2-x}$	–3.82	–2.94	–2.24	–2.52	–2.19

Table S4 Volume expansion degree of $MoSe_2$, Ti-$MoSe_2$, and Ti-$MoSe_{2-x}$ adsorbing Al^{3+} and $AlCl_4^-$.

Systems	$MoSe_2$ (%)	Ti-$MoSe_2$ (%)	Ti-$MoSe_{2-x}$ (%)
Al^{3+}	172	165	123
$AlCl_4^-$	229	224	198